**ROYAL SOCIETY OF CHEMISTRY**

## PAPER

Check for updates

# Versatile BODIPY dyes for advanced optoelectronics: random lasing, harmonics generation, and OLED application

Piotr Leśniak,†[a] Paulina Wójcicka, [iD] †[b] Adam Szukalski, [iD] *[b] Rafał Wysokiński, [iD] [c] Bouchta Sahraoui, [iD] [d] Dorota Zając,[b] Przemysław Kula,[a] Jarosław Myśliwiec [iD] [b] and Alina Szukalska [iD] *[b]

Organic optoelectronic materials are advancing rapidly, opening new possibilities for the design of efficient and multifunctional photonic systems. While most studies on boron-dipyrromethene (BODIPY) derivatives have focused on biomedical and sensing applications, their potential in advanced optoelectronics remains largely unexplored. Furthermore, previous reports have typically addressed single functionalities rather than integrated performance across diverse photonic regimes. Here, we introduce three newly synthesized BODIPY derivatives that demonstrate remarkable versatility as optically active materials. We demonstrate their nonlinear optical (NLO) activity through both second and third harmonic generation, supported by quantum chemical calculations. Moreover, these dyes exhibit strong amplified spontaneous emission and efficient random lasing without the need for external resonators, along with excellent photostability and compatibility in liquid crystalline and polymer matrices. Additionally, organic light-emitting diode (OLED) devices incorporating **BDP**s showed light emission, suggesting potential for further investigation. By combining stimulated emission, NLO, and OLED perspectives in one class of emitters, we provide a rare example of multifunctional organic materials. This versatility positions BODIPY dyes as promising candidates for integrated photonics and scalable optoelectronic technologies.

## 1. Introduction

In recent years, research in optoelectronics has progressed rapidly, particularly in the field of organic materials. Although inorganic systems remain highly valuable, they present several challenges. Careful material selection during growth and poor lattice compatibility complicate the fabrication process. Moreover, inorganic devices typically rely mostly on crystalline forms and require large-scale equipment under stringent conditions such as ultra-high vacuum. Addressing these limitations often demands substantial time, effort, and financial resources.[1–5] Thanks to advances in materials engineering and targeted synthesis, these limitations can now be addressed using organic compounds, which are flexible, widely accessible, and compatible with a variety of systems.[5,6] This enables the integration of diverse organic materials into scalable systems without the need for specialized equipment.

Fluorescent dyes constitute a key subgroup of organic materials, serving as emitting dopants and gain media in lasers.[7–11] These molecules are readily accessible, widely commercialized, and exhibit excellent emission properties, including high quantum yields of 0.56–0.98[12–15] and broad emission wavelength ranges.[16,17] Their favorable characteristics have driven extensive research in biological applications, such as fluorescent markers in medicine,[18,19] in photodynamic therapies (PDT)[18,20,21] as a fluorescent probe for gas or ion detection[18,22] and as chemical sensors.[23,24] Among these, boron-dipyrromethene (BODIPY), has attracted special attention, as it can be applied across all of the previously mentioned fields.[22,24] Less commonly, these compounds are utilized in optoelectronic applications, such as lasers and organic light-emitting-diode (OLED) devices. Accordingly, the following text focuses on BODIPY dyes and their unconventional applications in optoelectronics.

The family of BODIPY (Fig. 1) belongs to the class of organic fluorescent dyes, with fluorescence quantum yields in the range

[a] *Faculty of Advanced Technology and Chemistry, Military University of Technology, Warsaw, Poland*

[b] *Soft Matter Optics Group, Wroclaw University of Science and Technology, Wyb. Wyspiańskiego 27, 50-370 Wroclaw, Poland. E-mail: adam.szukalski@pwr.edu.pl, alina.szukalska@pwr.edu.pl*

[c] *Department of Analytical Chemistry and Chemical Metallurgy, Wroclaw University of Science and Technology, Wyb. Wyspiańskiego 27, 50-370 Wroclaw, Poland*

[d] *Univ Angers, LPHIA, SFR MATRIX, 2 Bd Lavoisier, F-49000 Angers, France*
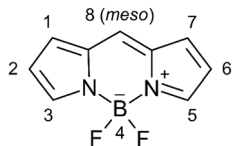
† Equal contribution.

Fig. 1 Chemical structure of BODIPY with IUPAC atom numbering.

of 0.86–1.00.[12,25–28] They are chemically and photostable, and tunable across emission wavelengths,[22,29] and relatively easy to synthesize[12] with low production costs. These combined advantages make BODIPY dyes excellent candidates not only for bio-related applications but also for optoelectronic technologies,[12,30,31] including laser systems,[29,32–36] NLO,[37–42] and OLEDs.[43–48] Despite extensive studies, most BODIPY derivatives have been explored for single-function applications, and their potential as multifunctional materials combining lasing, NLO activity, and electroluminescence remains largely unexplored. Here, we report newly synthesized BODIPY dyes that address this gap, demonstrating efficient performance across a range of laser spectroscopic studies as well as in OLED devices.

Firstly, we present computational and experimental NLO studies of three newly synthesized BODIPY dyes, namely **BDP1**, **BDP2**, and **BDP3**. Experiments reveal efficient second and third harmonic generation (SHG, THG, respectively). These results indicate that the compounds are promising candidates for NLO applications,[38] including frequency conversion,[49,50] optical switching,[51–53] and signal processing.[52,54] The empirical studies are complemented by quantum-chemical calculations, which demonstrate excellent NLO properties. In particular, **BDP2** exhibits significantly higher hyperpolarizability and ground-state dipole moments than $p$-nitroaniline derivatives, commonly used as reference models in spectroscopic studies.[55,56] Moreover, all **BDP**s exhibit efficient light emission and amplification when used

as laser dyes in these systems. Compared to traditional lasers, where the active medium is solid or gaseous, BODIPY-based random lasing (RL) systems are more compact, cost-effective, easier to fabricate and maintain, and provide a broader range of emission wavelengths. All these outstanding properties encouraged us to use BODIPYs in the construction of OLEDs, which we demonstrate in our studies as perspectives.

## 2. Results

### 2.1. Synthesis process

In this work, three BODIPY dyes with different aromatic substituents at the meso position were synthesized (Fig. 2), including two novel compounds, **BDP2** and **BDP3**, and **BDP1**, which was prepared following previously reported procedures.[57,58]

The target compounds were synthesized using the Lindsey-Wagner method, starting from the corresponding aldehydes.[59] The synthetic procedures are described in Section S1 (Fig. S1–S9) of the SI, including the preparation of the dyes and key intermediates, as well as their characterization by MS, ^{1}H NMR, and ^{13}C NMR spectroscopy. This method relies on a condensation reaction that occurs between electron-rich pyrroles and nucleophilic aldehydes to form dipyrromethanes. This is similar to the Rothemund reaction used for porphyrin synthesis,[60] but with the use of excess pyrrole (**1a**) or by blocking the second α position of the ring, the condensation can slow down after the dipyrromethane stage, limiting the formation of higher condensed products. Dipyrromethanes **2.1a** and **2.2a** were synthesised from the corresponding aldehydes using excess pyrrole (**1a**) and isolated with a 7.5% and 52% yield, respectively. The low yield of dipyrromethane **2.1a** was likely due to decomposition during the attempt to purify the compound by high vacuum distillation. For dipyrromethane **2.2a**, column chromatography afforded a
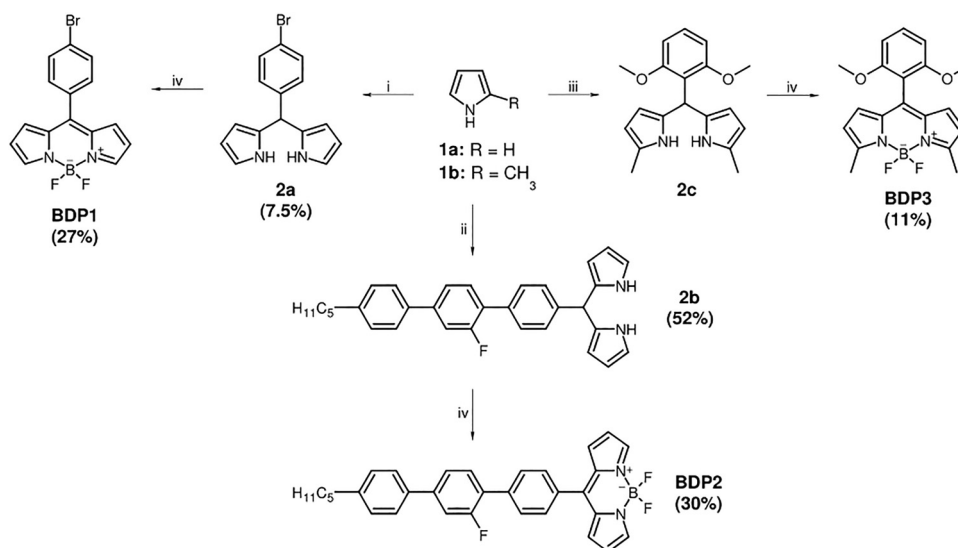


Fig. 2 Synthesis of BODIPY dyes **BDP1**, **BDP2**, and **BDP3**. Reagents and reaction conditions: (i) **1a**, 4-bromobenzaldehyde, TFA, r.t., 2.5 h; (ii) **1a**, 2′-fluoro-4″-pentyl-[1,1′;4′,1″-terphenyl]-4-carbaldehyde, TFA, r.t., 20 h; (iii) **1b**, 2,6-dimethoxybenzaldehyde, DCM, TFA, r.t., 20 h; (iv) DDQ, DCM, r.t., 0,25–1.5 h, then DIPEA, r.t., 5 min, then BF$_3$·Et$_2$O, 0 °C–r.t., 1.5–20 h.
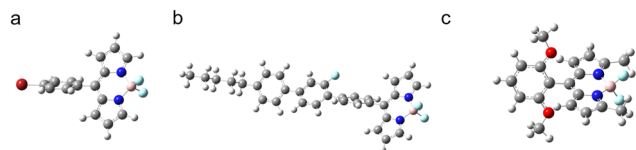
Fig. 3 Optimized ground-state geometries of the studied compounds: (a) **BDP1**, (b) **BDP2**, (c) **BDP3**.

higher yield. Using the known procedures,[59] the synthesised dipyrromethanes were then oxidized to transitional dipyrrins at room temperature using 2,3-dichloro-5,6-dicyano-1,4-benzoquinone (DDQ) in dichloromethane (DCM). After a short reaction time, a large excess of diisopropylethylamine (DIPEA) was added to the same reaction flask, followed by cooling and the addition of excess trifluoroboron in diethyl ether (BF$_3 \cdot$Et$_2$O). After reaction workup, **BDP1** and **BDP2** were isolated using column chromatography with a 27% and 30% yield, respectively. The synthesis of **BDP3** was done similarly, but starting from 2-methylpyrrole (**1b**) to limit side product formation during the dipyrromethane stage. This was used in an attempt to carry out the reactions in a "one-pot" fashion without the isolation of the dipyrromethane intermediate (**2b**). The condensation was carried out using the corresponding 2,6-dimethoxybenzaldehyde, and after standard DDQ oxidation, followed by boron complexation, the final product was purified using column chromatography and isolated with an 11% yield.

## 2.2. Quantum-chemical calculations

The following theoretical calculations, encompassing both linear and NLO properties, provide a predictive framework for comparison with the experimental results presented in Section 2.3. Nonlinear optical effects: SHG and THG.

Theoretical calculations were performed for the BODIPY derivatives, with their optimized ground-state geometries shown in Fig. 3(a)–(c).

These optimized structures served as the basis for all subsequent spectroscopic and NLO property predictions. In all studied structures, the S$_0 \rightarrow$ S$_1$ electronic transitions exhibit consistently strong oscillator strength values ($f \approx$ 0.64–0.71, Table 1), which is aligned with the high molar absorptivity of BODIPY derivatives ($\varepsilon >$ 70 000 M$^{-1}$ cm$^{-1}$) and their intense fluorescence even in aqueous and biological media.[61,62]

The absorption wavelengths predicted by theoretical calculations ($\lambda \approx$ 458–480 nm, Table 1, and spectra in SI, S2, Fig. S10) fall within the typical range reported for standard BODIPY derivatives (approximately 470–520 nm), which are well known for their characteristic absorption maxima in the blue-green region of the spectrum.[62]

Table 2 Calculated energies of Frontier molecular orbitals ($E_{HOMO}$, $E_{LUMO}$) and molecular orbital energy gap ($\Delta E^{FMO}$)

| Compound | $E_{HOMO}$ (eV) | $E_{LUMO}$ (eV) | $\Delta E^{FMO}$ (eV) |
|---|---|---|---|
| **BDP1** | −7.015 | −2.718 | 4.297 |
| **BDP2** | −6.980 | −2.686 | 4.293 |
| **BDP3** | −6.498 | −2.352 | 4.146 |

Particularly noteworthy is **BDP3**, which displays the largest red shift in absorption and the lowest HOMO–LUMO energy gap (4.15 eV, Table 2).

This behaviour is consistent with reported observations for structurally extended BODIPYs bearing donor–acceptor substituents (see frontier molecular orbitals in Fig. 4a–c).[24,61]

Regarding the Stokes shift, the highest values (up to 20 nm) were observed for **BDP3**, indicating greater geometrical reorganization in the excited state (highest root-mean-square deviation (RMSD), SI, S3, Fig. S11). This is consistent with literature reports attributing shifts of 10–30 nm to charge-transfer (CT) effects or molecule-environment interactions.[24,61,62] For **BDP2**, which shows the highest change in dipole moment ($\Delta\mu =$ 1.96 D), the HOMO $\rightarrow$ LUMO transition may possess partial CT character – this has also been reported for systems with donor groups in the *meso* position (Fig. 4b).[63,64] Notably, **BDP1**, characterized by the smallest $\Delta\mu$ and the smallest Stokes shift, resembles classical, rigid BODIPY systems. Such molecular arrangements are described in the literature as optimal candidates for fluorescent labeling due to their high quantum stability and minimal geometrical reorganization.[20] The theoretical data are consistent with experimental observations for both basic and functionalized BODIPY dyes. The distribution of $\Delta\mu$ and $\Delta\lambda^{Stokes}$ parameters correlates well with the type of substituents and the degree of molecular rigidity. **BDP3** exhibits features typical of dyes with potential for optoelectronic applications (*e.g.*, OLEDs), whereas **BDP1** appears most suitable for biological applications, where high stability and minimal spectral shifts are required.

The NLO properties of the three studied BODIPY systems were assessed through the calculated first ($\beta_{tot}$) and the average second hyperpolarizability ($\gamma_{avg}$) (see Table 3).

**BDP2** exhibits the highest $\beta_{tot}$ value, which can be attributed to the presence of a more effective donor–$\pi$–acceptor system and greater charge delocalization in the excited state. The $\beta_{tot}$ for **BDP2** reaches 17 174 a.u., corresponding to $\sim$1.49 $\times$ 10$^{-28}$ esu, which is comparable to classical NLO dyes such as DANS ($\beta \approx$ 55–70 $\times$ 10$^{-30}$ esu) or stilbene derivatives with strong donor and acceptor groups.[65] For comparison, the $\beta_{tot}$ value for **BDP1** is 393 a.u. ($\sim$7 $\times$ 10$^{-30}$ esu), which corresponds to typical

Table 1 Calculated one-photon absorption parameters for the **BDP** compounds: vertical excitation energies ($E$), oscillator strengths ($f$), ground- and excited-state dipole moments ($\mu_G$, $\mu_E$), and Stokes shift ($\Delta\lambda^{Stokes}$). All data refer to the S$_0 \rightarrow$ S$_1$ transition

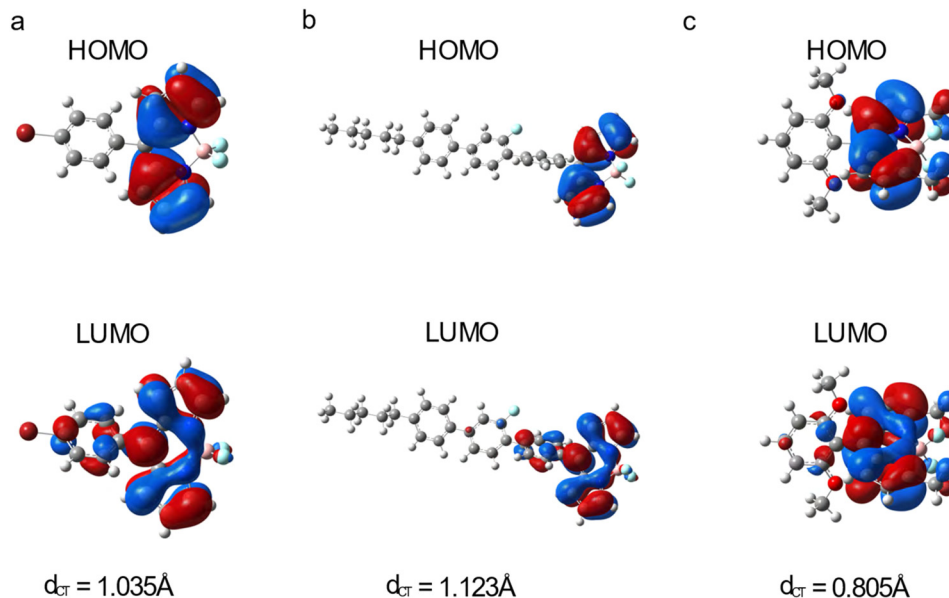| Compound | $\lambda$ (nm) | $E$ (eV) | $f$ (−) | $|\mu_G|$ (D) | $|\mu_E|$ (D) | $\Delta\mu = |\mu_E| - |\mu_G|$ (D) | $\Delta\lambda^{Stokes}$ (nm) |
|---|---|---|---|---|---|---|---|
| **BDP1** | 459 | 2.703 | 0.654 | 5.27 | 3.58 | 1.69 | 17 |
| **BDP2** | 458 | 2.706 | 0.644 | 9.97 | 8.01 | 1.96 | 17 |
| **BDP3** | 480 | 2.584 | 0.705 | 7.84 | 6.59 | 1.25 | 20 |

**Fig. 4** Frontier molecular orbitals (HOMO and LUMO) involved in the lowest-energy one-photon transition ($S_0 \rightarrow S_1$) for (a) **BDP1**, (b) **BDP2**, and (c) **BDP3**. The distance between the barycenters of electron density transfer.

**Table 3** Total first hyperpolarizability ($\beta_{tot}$), average second hyperpolarizability ($\gamma_{avg}$) at the static and dynamic ($\lambda$ = 1064 nm) regime, and $\beta$-electric field induced second harmonic generation ($\beta_{EFISH}$) for **BDP1–3**

| | $\beta_{tot}^0$ (a.u.) | $\beta_{tot}^{1064}$ (a.u.) | $\gamma_{avg}^0$ (a.u.) | $\gamma_{avg}^{1064}$ (a.u.) |
|---|---|---|---|---|
| **BDP1** | 393 | 116 | 25 398.06 | 353 874.40 |
| **BDP2** | 17 174 | 39 055 | 375 027.96 | 5 692 689.93 |
| **BDP3** | 13 346 | 18 582 | −6948.57 | 225 633.30 |

values for symmetric π-conjugated systems such as nitroaniline or azobenzenes.[66] The value obtained for **BDP3** – 13 346 a.u. ($\sim 4 \times 10^{-28}$ esu) – suggests a balanced donor–acceptor effect and moderate electronic anisotropy, comparable to selected BODIPY derivatives modified at the *meso* position.

To evaluate the potential of the investigated molecules for NLO applications, particularly for SHG, the $\beta_{EFISH}$ parameter $\sim \mu \cdot \beta_{tot}$ for **BDP2** was analysed. This parameter directly corresponds to the measurable signal in the electric field induced second harmonic generation (EFISH) technique, which is widely employed to assess the NLO properties of organic compounds in solution.[67–69] These values suggest that **BDP2** possesses particularly high NLO potential ($\beta_{EFISH} = 5.82 \times 10^{-28}$ esu), significantly exceeding that of classical compounds such as *p*-nitroaniline derivatives ($8–21 \times 10^{-30}$ esu) or DANS ($\sim 55 \times 10^{-30}$ esu).[70,71]

The calculated second hyperpolarizability values ($\gamma_{avg}$) for the studied **BDP** compounds reveal significant differences among the molecules and a pronounced dispersion effect. In particular, **BDP2** exhibits a substantial increase in $\gamma$ at a wavelength of 1064 nm, indicating an enhancement of the NLO response under dynamic conditions This enhancement may be linked to near-resonant optical or two-photon effects, characteristic of systems with pronounced charge-transfer (CT) character. Although the photon energy employed in the dynamic

calculations (1064 nm, 1.165 eV) is below the electronic excitation energies of the molecules, two-photon processes could still contribute to the observed enhancement of NLO responses. The obtained values highlight the potential of **BDP2** as an active material for NLO applications.[61]

The calculated absorption properties of the studied BODIPY derivatives show good consistency with their potential NLO responses. **BDP1**, with an absorption maximum at 459 nm and a modest dipole moment change upon excitation ($\Delta\mu$ = 1.69 D), represents a classical, rigid BODIPY core with minimal CT character. This is reflected on its low $\beta_{tot}$ value, in agreement with literature reports for symmetric π-conjugated systems.[68,71] In contrast, **BDP2**, with a similar absorption wavelength (458 nm), but the highest $\Delta\mu$ value (1.96 D) and an extended π-conjugated system, results in significantly higher $\beta_{tot}$ and $\beta_{EFISH}$ parameters. These findings indicate an efficient CT character, typical of push–pull systems with extended π-conjugation.[72–74] **BDP3**, on the other hand, is characterized by a red-shifted absorption maximum (480 nm) and an intermediate $\Delta\mu$ value (1.25 D), displaying NLO properties that lie between those of **BDP1** and **BDP2**. The presence of methoxy groups in **BDP3** likely introduces a localized CT character, which justifies the moderately high $\beta_{tot}$ value observed.[64,75] The next section focuses on the experimental SHG and THG responses of the studied compounds to evaluate predicted trends. In the SI (S3, Tables S1–S5), we provide supporting data, including the calculated second- and third-order hyperpolarizability tensor components in both static and frequency-dependent regimes, as well as the full Cartesian coordinates of the optimized structures.

### 2.3. Nonlinear optical effects: SHG and THG

The NLO activity of the investigated BODIPYs was further confirmed through SHG and THG experiments, with the
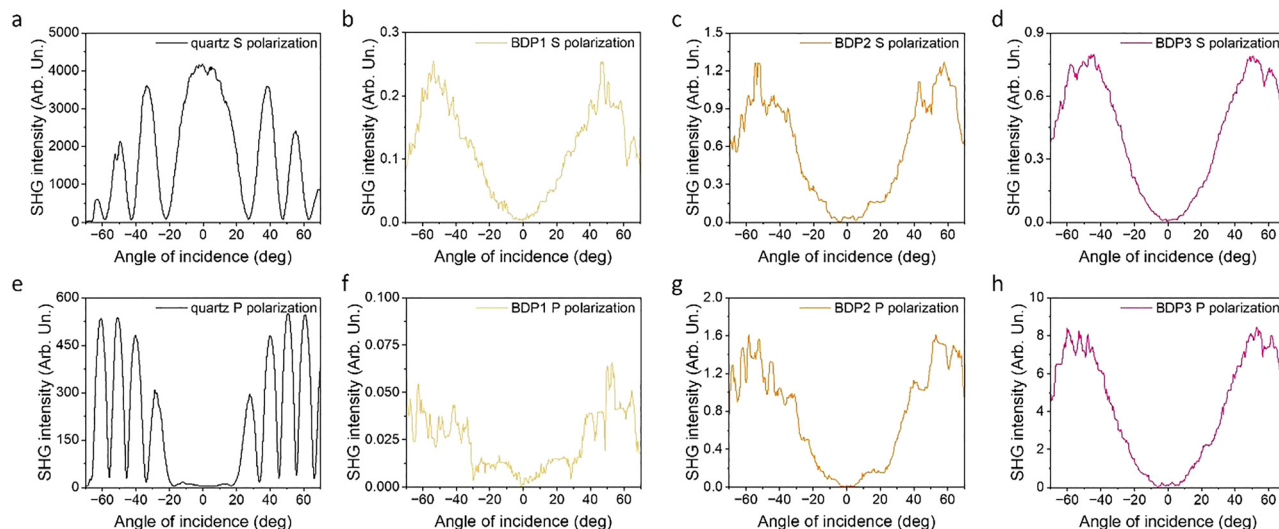
Fig. 5 Maker fringes representing SHG signals recorded in two orthogonal polarizations: *S* (a)–(d) and *P* (e)–(h), for quartz (a, e), **BDP1** (b, f), **BDP2** (c, g), and **BDP3** (d, h), respectively.

corresponding results presented in Fig. 5 and 6, respectively. Since the studied molecules are centrosymmetric, deliberate symmetry breaking was necessary to induce SHG. This was accomplished using corona poling, a thermo-electric technique that generates non-centrosymmetry in the samples. Angular-dependent SHG signals were recorded and are displayed as characteristic Maker fringes in Fig. 5a–h. SHG measurements were analysed using a comparative approach based on the Lee model, starting with a quartz reference measured under two orthogonal polarization configurations, *S* and *P* (Fig. 5a and e).
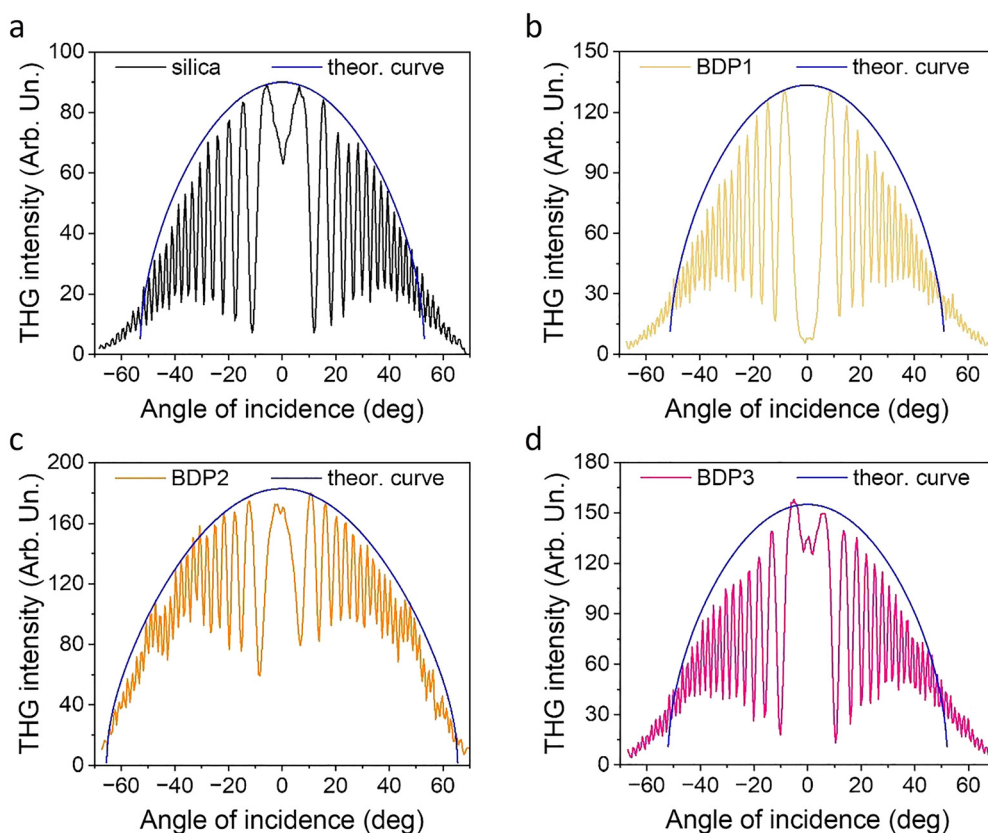


Fig. 6 Maker fringes representing THG signals, shown alongside theoretical model curves (blue solid lines), for silica (a), **BDP1** (b), **BDP2** (c), and **BDP3** (d), respectively.

Additionally, since quartz is a strongly anisotropic material with respect to *S*-polarization, and the samples exhibit enhanced signals under *P*-polarization, we decided to adjust the experimentally determined $\chi^{(2)}$ values obtained for the *P*-polarization configuration by applying a Fresnel factor correction.[76,77] This correction was introduced because the calculated second-order susceptibility could otherwise be over- or underestimated, depending on the polarization used (*S* or *P*) when quartz is employed as the reference material. Subsequently, all three BODIPY derivatives were investigated under identical conditions. In each case, the SHG signal exhibited pronounced modulation as a function of the incident angle of the fundamental laser beam. Among the series, **BDP1** exhibited the lowest 2nd order NLO response, with $\chi^{(2)}$ values of 0.063 and $\chi^{(2)}_{\mathrm{eff}}$ of 0.749 pm V$^{-1}$ for *S* and *P* polarizations, respectively. **BDP2** demonstrated the highest response in *S*-polarization ($\chi^{(2)}$ = 0.136 pm V$^{-1}$), while **BDP3** exhibited the strongest performance under *P*-polarization, reaching $\chi^{(2)}_{\mathrm{eff}}$ = 2.447 pm V$^{-1}$, approximately 2.5 times higher than the quartz reference ($\chi^{(2)}$ = 1.0 pm V$^{-1}$).[78] Although the overall SHG signals were modest, the sensitivity to molecular structure and angular variation underscores the potential of BODIPY systems in 2nd order nonlinear optics. A detailed summary of the extracted $\chi^{(2)}$ and $\chi^{(2)}_{\mathrm{eff}}$ values is provided in Table 4.

The 3rd order NLO properties of the BODIPY compounds were subsequently investigated, with the results displayed in Fig. 6a–d. The recorded signals exhibited Maker fringe patterns, characteristic of phase-matched harmonic generation, but at higher frequencies than those of SHG. Fused silica served as the reference material, while data analysis and extraction of 3rd order susceptibilities ($\chi^{(3)}$) were performed using the Kubodera–Kobayashi theoretical model.

In contrast to the SHG measurements, the THG response from the studied BODIPYs was pronounced even without any symmetry-breaking treatment, underscoring the intrinsic 3rd order NLO activity of these centrosymmetric molecules. All compounds exhibited $\chi^{(3)}$ values exceeding that of the silica reference ($\chi^{(3)}$ = 2.0 × 10$^{-22}$ m$^2$ V$^{-2}$).[79] Among them, **BDP1** showed the weakest response, with $\chi^{(3)}$ = (3.698 ± 0.024) × 10$^{-22}$ m$^2$ V$^{-2}$. **BDP3** demonstrated an enhanced value of (4.116 ± 0.024) × 10$^{-22}$ m$^2$ V$^{-2}$, while **BDP2** exhibited the strongest 3rd order response, reaching (5.190 ± 0.032) × 10$^{-22}$ m$^2$ V$^{-2}$, approximately 2.5 times higher than the silica benchmark.

These findings highlight the strong 3rd order NLO potential of BODIPY-based materials, achieved without requiring external poling or symmetry manipulation. This stands in contrast to SHG, which requires symmetry-breaking techniques to activate 2nd order responses. A comprehensive overview of the $\chi^{(3)}$ values, along with the morphological characteristics of the samples, is provided in Table 4.

When comparing the $\chi^{(3)}$ values obtained in this study with those reported in the literature for BODIPY-based materials,[80] it is essential to consider differences in sample composition and experimental conditions. Literature values typically range from approximately 5.0 × 10$^{-20}$ to 1.3 × 10$^{-19}$ m$^2$ V$^{-2}$ (SI units), measured in polymer films containing significantly higher chromophore concentrations, up to 30% w/w in polystyrene matrices. In contrast, the BODIPY compounds investigated here were incorporated at a substantially lower concentration of 2% w/w in polymethyl methacrylate (PMMA), yet still exhibit significant 3rd order nonlinear susceptibilities. Furthermore, the reported studies employed nanosecond pulsed lasers, which can induce thermal effects and free-carrier generation, potentially leading to artificially enhanced $\chi^{(3)}$ values. The present measurements utilized a picosecond pulsed laser, minimizing such thermal contributions and providing a more intrinsic evaluation of the 3rd order NLO response of the BODIPY chromophores.

Notably, a recent study employing a comparable experimental setup with approximately 5% dye concentration reported 2nd order nonlinear coefficients ($\chi^{(2)}$) in *S* polarization of 2.75 and 5.86 pm V$^{-1}$ for BODIPYs B1 and B2, respectively, and in *P* polarization of 3.61 and 5.42 pm V$^{-1}$.[40] Their 3rd order nonlinear susceptibilities ($\chi^{(3)}$) were found to be 3.2 × 10$^{-21}$ and 1.79 × 10$^{-20}$ m$^2$ V$^{-2}$ for B1 and B2, respectively, which are higher than those obtained in this work, consistent with their higher dye loading and material-specific properties. This comparison highlights the impact of dye concentration and molecular structure on the NLO response.

These factors collectively explain the observed lower $\chi^{(3)}$ magnitudes in this work, while highlighting the robustness and relevance of the results under more controlled, low-concentration, and low-thermal-loading conditions. A detailed summary of the 2nd and 3rd order susceptibilities alongside morphological parameters is presented in Table 4.

**Table 4** Summary of the 2nd and 3rd order nonlinear optical susceptibilities, along with morphological characteristics, of the measured and cited BODIPY compounds

| Compound | Dye conc. *vs.* polymer mass %(w/w) | Thickness (nm) | $\alpha$ at 355 nm (cm$^{-1}$) | $\chi^{(3)}$ × 10$^{-22}$ (m V$^{-1}$)$^2$ | $\Delta\chi^{(3)}$ × 10$^{-22}$ (m V$^{-1}$)$^2$ | $a$ at 532 nm (cm$^{-1}$) | $\chi^{(2)}$ *S* pol. (pm V$^{-1}$) | $\chi^{(2)}_{\mathrm{eff}}$ *P* pol. (pm V$^{-1}$) |
|---|---|---|---|---|---|---|---|---|
| **BDP1** | **2.0** | **1544** | **2042.09** | **3.698** | **0.024** | **388.23** | **0.063** | **0.749** |
| **BDP2** | **2.0** | **1622** | **556.04** | **5.190** | **0.032** | **204.61** | **0.136** | **1.102** |
| **BDP3** | **2.0** | **1681** | **669.04** | **4.116** | **0.024** | **1295.89** | **0.107** | **2.447** |
| **2a**[80] | 30.0 | 77–170 | 63 000 | 500 | — | — | — | — |
| **1a**[80] | 30.0 | 77–170 | 82 000 | 1300 | — | — | — | — |
| **B1**[40] | ~5.0 | 30–1200 | — | 32 | — | — | 2.75 | 3.61 |
| **B2**[40] | ~5.0 | 30–1200 | — | 179 | — | — | 5.86 | 5.42 |
| Silica | — | — | — | 2.0 | 0.2 | — | — | — |
| Quartz | — | — | — | — | — | — | 1.0 | 1.0 |

The experimental SHG and THG measurements are in good agreement with the quantum-chemical predictions: **BDP2** consistently displays the strongest third-order NLO response, while **BDP1** remains the weakest across all methods. Notably, the particularly strong SHG activity of **BDP3** under *P*-polarization suggests additional structural and orientational factors not fully captured by the theoretical models, underscoring the complementarity of computational and experimental approaches. These findings establish a direct correlation between molecular structure, calculated NLO parameters, and experimental responses, which will be further explored in the context of spectroscopic properties and RL performance in the following section.

## 2.4. Basic spectroscopic properties and RL performance

Beyond their NLO activity, the fundamental spectroscopic properties of the studied BODIPY derivatives were investigated to provide a comprehensive overview of their photophysical behaviour. Absorption and fluorescence spectra of all **BDP**s, measured in LC and PMMA matrices, are presented in Fig. 7. Corresponding studies in solution (DCM) are provided in the SI (Section S4, Fig. S12), along with Table S6 summarizing the relevant optical properties.

The absorption and emission spectra of the studied BODIPY derivatives show similar spectral ranges in both LC (E7) and PMMA matrices, allowing for a straightforward comparison of
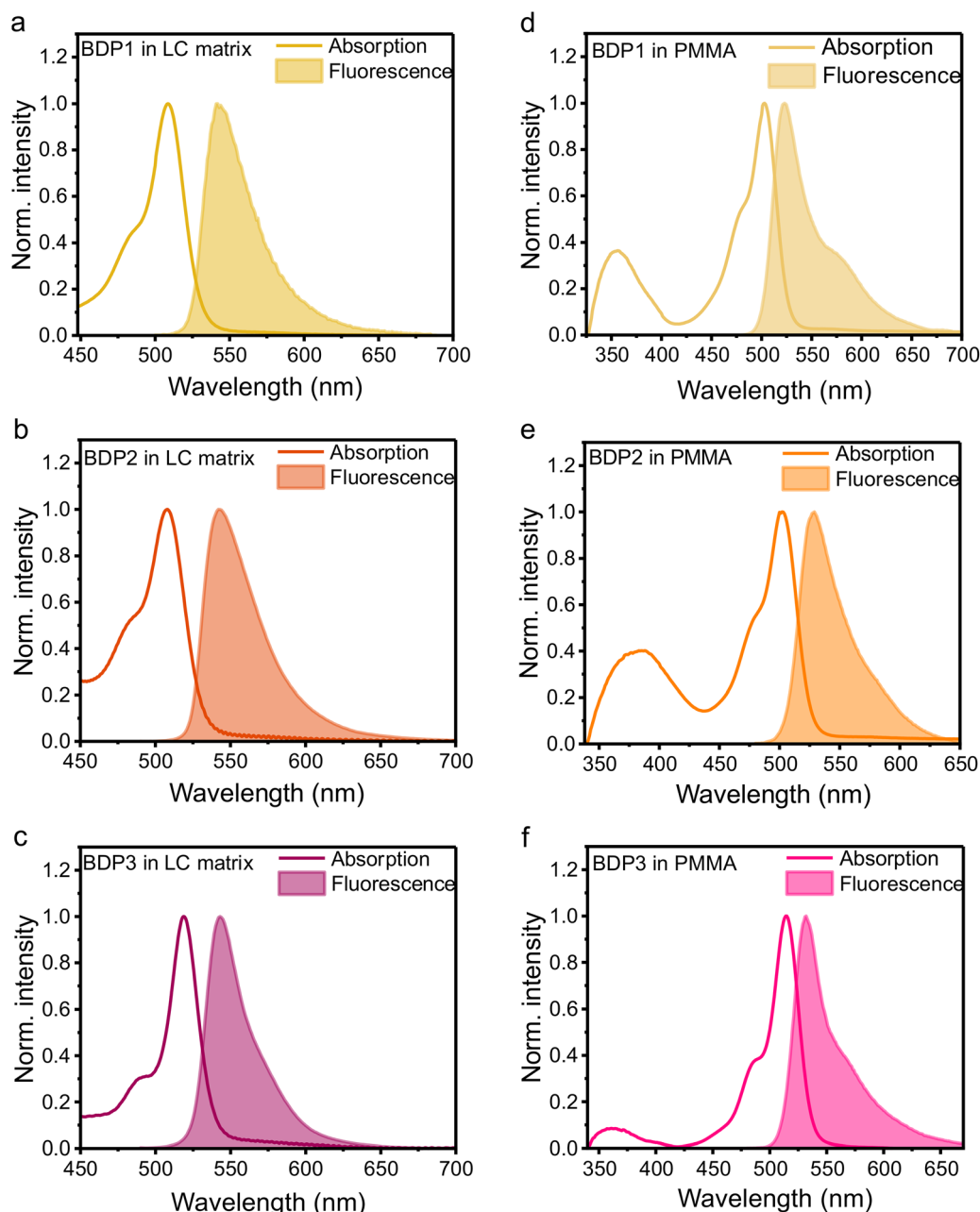


Fig. 7 The absorbance (lines) and emission (coloured areas) spectra of the investigated BODIPY dyes doped to the LC (a–c) PMMA matrix (d–f).

their photophysical behaviour in different environments. In the LC environment, the absorption range spans 450–550 nm, with maximum peaks at 508 nm, 507 nm, and 518 nm for **BDP1**, **BDP2**, and **BDP3**, respectively (Fig. 7a–c). In contrast, the PMMA-doped thin films exhibit a broader absorption range, from 335 nm to 550 nm, and show additional peaks likely associated with $S_0 \rightarrow S_2$ transitions. Maximum absorption peaks in PMMA were observed at 502 nm, 501 nm, and 514 nm, for **BDP1–3**, respectively (Fig. 7d–f).

Fluorescence spectra for BODIPY in the LC matrix extend from 500 to 650 nm, with peak maxima at 541 nm, 542 nm, and 543 nm for **BDP1**, **BDP2**, and **BDP3**, respectively (Fig. 7a–c). In PMMA, the fluorescence range is slightly broader, from 490 to 660 nm, peaking at 523 nm, 528 nm, and 532 nm, for **BDP1–3**, accordingly (Fig. 7d–f). The red shift in emission observed within the LC matrix may be attributed to the polarity of the anisotropic environment, which is further pronounced by the dense packing of the molecules, which efficiently stabilizes the excited state, shifting the emission towards longer wavelengths compared to the isotropic environments of DCM (see SI, S4). However, in the examined PMMA-based systems, the postulated rigidity might be even greater than in LC according to combined polarizability and molecular packing effects, which results in lower energetic excited states. Considering measurements in DCM, all of the synthesised BODIPY dyes exhibit absorption/emission spectra characteristics (SI, S4, Fig. S12 and Table S6), which are similar to those of the unsubstituted BODIPY,[62] indicating the little influence *meso*-phenyl substituents have on the electronic structure of the core. The photophysical parameters for the synthesized dyes in DCM are presented in SI, S4, Table S6. As demonstrated, the most intense absorption bands, at 503 nm, 502 nm, and 515 nm, correspond to the $S_0 \rightarrow S_1$ transitions of **BDP1–3** dyes, respectively. For **BDP1** and **BDP2**, the values of peak maximum are similar, but for **BDP3**, there is a slight shift of the band. This is caused by the presence of methyl substituents in the 3,5-positions, which, through inductive effects and $\sigma$–$\pi$ hyperconjugation, donate electron density to the BODIPY core. This leads to stabilization of the excited state and a decrease in its energy, resulting in a redshift of the absorption and emission bands.[81] Among the synthesized compounds **BDP3** has the highest quantum yield of fluorescence in DCM (0.66). The significantly lower $\phi_{fDCM}$ (0.02) observed for **BDP2** may be attributed to the possibility of free rotation of the BODIPY core in relation to the terphenyl ring system.[82] For **BDP1** the $\phi_{fDCM}$ value (0.004) is even lower, which may result from the heavy atom effect caused by the presence of a bromine atom, as well as free rotation of the bromophenyl ring. The highest $\phi_{fDCM}$ value (0.66) obtained for **BDP3** confirms the effectiveness of *ortho*-methoxy groups in restricting ring rotation. Interestingly, in rigid PMMA films, the fluorescence quantum yields ($\phi_{fPMMA}$) of the three BODIPY derivatives increase substantially, reaching 0.45 for **BDP1**, 0.27 for **BDP2**, and 0.88 for **BDP3**. These values represent a dramatic enhancement compared to the solution, suggesting that rigid environments strongly suppress non-radiative relaxation channels, favouring more efficient emission. This trend is expected to directly impact the lasing behaviour discussed in the following sections, since higher fluorescence

quantum efficiency is generally correlated with lower lasing thresholds and improved operational stability.

After characterizing the absorption and fluorescence properties of the BODIPY derivatives in DCM solution as well as in LC and PMMA matrices, their potential for stimulated emission was investigated, leading to the observation of light amplification. The stimulated emission spectra and estimated energy thresholds for the studied dyes in LC (Fig. 8a–f) and PMMA (Fig. 8g–l) matrices are presented below.

For all three BODIPY derivatives in both matrices, emission was observed in the green region of the spectrum (530–570 nm). As the pump energy increased, a systematic reduction in the full width at half maximum (FWHM) was observed for all samples (Fig. 8a–f). A comparison of the FWHM values between the stimulated emission spectra at maximum excitation energy and the corresponding fluorescence spectra is provided and discussed in the SI (Section S5, Table S7).

Distinct RL behaviour, characterized by the appearance of sharp and well-defined modes, was identified in the emission spectra of the samples shown in Fig. 8b, e and f. In contrast, the stimulated emission from the samples in Fig. 8a and c displayed features more characteristic of amplified spontaneous emission (ASE), where only spectral narrowing without discrete lasing modes was observed. The classification, therefore, stems from the spectral shape: ASE corresponds to smooth emission bands with reduced FWHM (SI, S5, Table S7), whereas RL is confirmed by multimodal structures. For LC, the thresholds, designated with the light-in/light-out (Li–Lo; see Methods), were 259 μJ for **BDP1** (Fig. 8g), 145 μJ for **BDP2** (Fig. 8h), and 188 μJ for **BDP3** (Fig. 8i). In PMMA, the thresholds were significantly lower: 96 μJ for **BDP1** (Fig. 8j), 65 μJ for **BDP2** (Fig. 8k), and 158 μJ for **BDP3** (Fig. 8l). When compared in pairs, it is clear that for each dye the threshold in PMMA is consistently lower than in LC: approximately 2.7 times lower for **BDP1**, 2.2 times lower for **BDP2**, and 1.2 times lower for **BDP3**. This trend reflects the higher rigidity of the polymeric environment, which enhances quantum efficiency by suppressing non-radiative relaxation. Consequently, PMMA hosts provide a more favourable platform for low-threshold lasing than LC systems, particularly for **BDP1** and **BDP2**. **BDP2** exhibits the lowest lasing threshold, consistent with its strong push–pull character. As shown in Table 1 and Fig. 4, it has the largest ground- to excited-state dipole moment difference ($\Delta\mu$ = 1.96 D) and the greatest HOMO–LUMO charge-transfer distance ($d_{CT}$ = 1.123 Å), indicating the most efficient intramolecular charge separation. Its high calculated first and second hyperpolarizabilities (Table 3) further reflect a highly polarizable electronic structure, promoting optical gain by reducing nonradiative losses and facilitating population inversion. Importantly, the obtained threshold values are not only lower than those observed in LC matrices, but they also compare very favourably with previously reported thresholds for other organic dye lasers, placing these BODIPY-based systems among the efficient low-threshold organic gain media reported to date.[36,83] Moreover, in the context of comparing these specifically to other BODIPY derivatives, various publications report laser threshold energies around 0.8 mJ.[84–87] In another study,

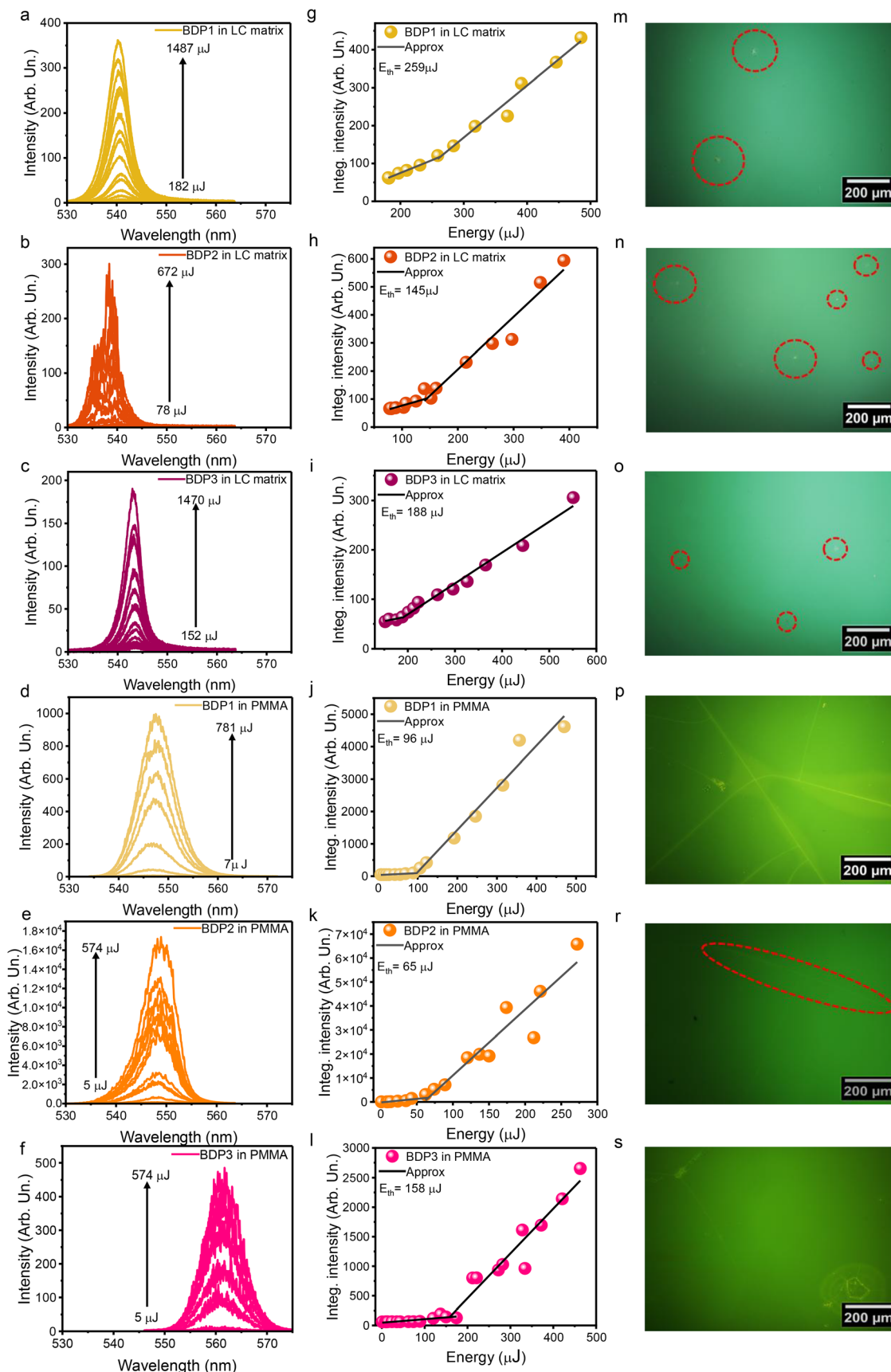**Fig. 8** The lasing spectra of BODIPY dyes in LC (a)−(c), and PMMA (d)−(f). The lasing thresholds for all measured systems (g)−(l). Morphological studies with the use of fluorescence microscopy in all samples ($\lambda_{exc}$ = 360 nm); (m)−(s).

thresholds of 0.36 mJ, and subsequently 0.6, up to 1.1 mJ, were obtained respectively.[88] The fluorescence-lasing inflection values in the range of 0.19–1.8 mJ[89] for boron-substituted BODIPY dyes can be also found.

It is therefore essential to complement the spectral analysis with a direct examination of sample morphology, as the presence and distribution of scattering centers provide crucial information about the underlying feedback mechanism. In the LC matrices, microscopic images show only a few small aggregates or crystallites for **BDP1** (Fig. 8m) and **BDP3** (Fig. 8o), whereas **BDP2** (Fig. 8n) contains a much larger number of such structures distributed throughout the volume. These observations support the spectral classification: ASE dominates in **BDP1** and **BDP3** due to the low density of scattering centers, while the higher aggregate density in **BDP2** provides the conditions necessary for constructive feedback, resulting in RL.

For BODIPY-doped PMMA films, stimulated emission was consistently assigned to RL across all samples. In these thin films, the microscopic analysis reveals a dense distribution of scattering centres, ranging from aggregates to well-developed microcrystals, as well as highly characteristic micro-crack pathways observed under fluorescence microscopy (Fig. 8p–s). All these morphological features, formed within the polymer matrix, contribute to enhanced light scattering and feedback. It results in more coherent lasing, as RL requires the presence of multiple constructive scattering centres[90] formed by the host/guest interactions to further amplify light. Additional microscopic inspection in bright field performed with a Nikon ECLIPSE Ti2-E inverted microscope (see SI, Section S6 and Fig. S13) further confirms the observations for both BODIPY-PMMA and BODIPY-LC systems. The images reveal pronounced surface irregularities, microcrack networks, and crystalline domains up to tens of micrometres in size, all contributing to the dense scattering centers responsible for the RL feedback in PMMA. In the LC samples, a markedly higher density of larger aggregates is observed for **BDP2** compared to **BDP1** and **BDP3**, providing the structural inhomogeneity necessary for efficient scattering and the onset of RL.

To quantify matrix-induced spectral shifts, we calculated the Stokes shifts (maximum fluorescence – maximum absorption) and compared absorption maxima with lasing maxima (see SI, S7, Table S8). In LC, the Stokes shifts are 33 nm (**BDP1**), 35 nm (**BDP2**), and 25 nm (**BDP3**), whereas in PMMA they are 21 nm (**BDP1**), 27 nm (**BDP2**), and 18 nm (**BDP3**). Lasing maxima relative to absorption are close to the Stokes shifts in LC ($\Delta \approx$ 25–32 nm) and nearly coincident with the fluorescence maxima (difference $\leq$ 4 nm), indicating that stimulated emission in LC originates from the same emissive states as steady-state fluorescence. In PMMA, however, lasing maxima are substantially red-shifted with respect to both absorption and fluorescence ($\Delta$(lasing-fluorescence) $\approx$ +20–29 nm for **BDP1–3**). This pronounced red-shift in PMMA likely reflects the combined influence of increased local rigidity, aggregate/microcrystal formation, and possible self-absorption/selection effects in the polymer films, which produce emission from lower-energy emissive sites and/or spectrally selective feedback. We therefore conclude that the matrix modifies not only the absolute spectral positions but also the effective Stokes behaviour observed under stimulated emission; these distinctions should be considered when selecting host media for targeted lasing wavelengths and low-threshold operation.

Finally, photostability measurements were carried out for both matrices, with the results shown in Fig. 9. These data confirm the operational stability of the systems under continuous excitation.

RL photostability of all BODIPY derivatives was assessed at pump energies approximately 1.5–2 times above the lasing threshold (Fig. 9a–f). For **BDP1** and **BDP3**, the LC matrix significantly enhanced photostability: the emission intensity dropped to 50% after 1911 (Fig. 9a) and 1930 laser pulses (Fig. 9c), respectively, whereas in polymer matrices, the corresponding values were 751 (Fig. 9d) and 819 (Fig. 9f) pulses. In contrast, **BDP2** exhibited greater stability in the polymer environment, with 4909 pulses to reach 50% emission (Fig. 9e), compared to only 647 pulses in the LC matrix (Fig. 9b). These observations indicate that the photostability of RL emission is strongly dependent on the interplay between molecular structure and the matrix environment. In particular, the rigid polymer matrix enhances stability for **BDP2** by suppressing non-radiative relaxation, while for **BDP1** and **BDP3**, the LC domains appear to provide more favourable stabilization. Overall, the measured lifetimes are consistent with those typically reported for organic fluorescent dyes.[36,91] The most resilient sample was found to be **BDP2** in PMMA.

## 2.5. Perspectives – OLEDs

Preliminary experiments were conducted to evaluate the potential of BODIPY derivatives in simple OLED structures. The single-layer devices were fabricated following a procedure detailed in the Methods section to evaluate the individual potential of BODIPYs and also for reliable comparison with the poly[2-methoxy-5-(2-ethylhexyloxy)-1,4-phenylenevinylene] (MEH-PPV): BODIPY-doped films (2 wt%), respectively. The simple device also incorporated indium tin oxide (ITO) as the anode, poly(3,4-ethylenedioxythiophene):poly(styrenesulfonate) (PEDOT:PSS) as the hole injection layer, and eutectic gallium–indium alloy (GaIn) as the cathode.

Therefore, the OLED structure employed consisted of either ITO/PEDOT:PSS/BODIPY/GaIn or ITO/PEDOT:PSS/MEH-PPV/BODIPY/GaIn. The energy level diagrams with indicated OLED components of the complete devices (both where only BODIPY as well as together with MEH-PPV layer applied) are presented in Fig. 10a and b, respectively. In these configurations, PEDOT:PSS was used as the hole injection layer due to its highest occupied molecular orbital (HOMO) being closely aligned with the work function of the ITO electrode.

Eutectic gallium–indium (GaIn), a liquid metal with a work function of approximately −4.2 eV, served as the cathode. One advantage of using GaIn is that it eliminates the need for metal evaporation during the device fabrication process.[92] Photos illustrating the electroluminescence phenomenon collected during investigations on OLED performance with 'pure' and MEH-PPV-functionalized **BDP2** are shown in Fig. 10a and b as insets.
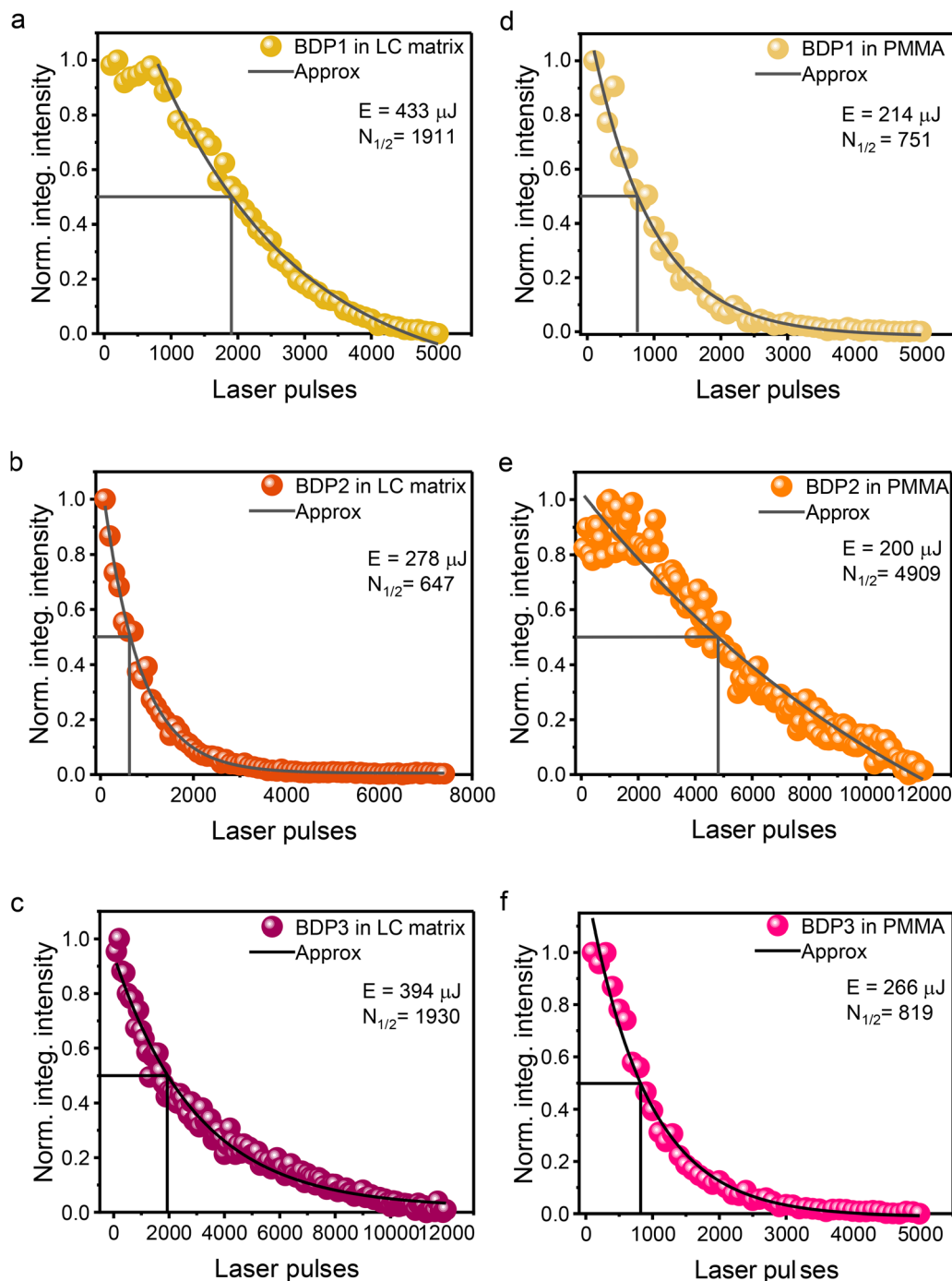
**Fig. 9** RL photostability of the BODIPY dyes in LC (a)–(c), and PMMA (d)–(f) matrices.

A typical current–voltage ($I$–$V$) characteristics of the well-known MEH-PPV-based OLED is shown in Fig. 10c. In OLEDs, electrons are injected from the cathode and holes from the anode. In this case, ITO functioned as the anode, while GaIn acted as the cathode. CT in the organic layers occurs primarily through hopping mechanisms along the polymer chains. Recombination of electrons and holes within the emissive layer depends on the charge carrier mobilities and the thickness of that layer. The color of emitted photons is determined by the energy gap between the HOMO and the lowest unoccupied molecular orbital (LUMO) of the electroluminescent material.[93,94] For that reason, the observed emission colours of the MEH-PPV-based OLED (Fig. 10d), but also pure **BDP2**-based OLED (Fig. 10a inset), and finally ITO/PEDOT:PSS/MEH-PPV/BDP2/GaIn (Fig. 10b inset) are slightly different, which is clearly visible. The similar current–voltage characteristics for the investigated **BDP1** and **BDP3** are shown in the SI (S8, Fig. S14). Although $I$–$V$ characteristics were recorded only in a
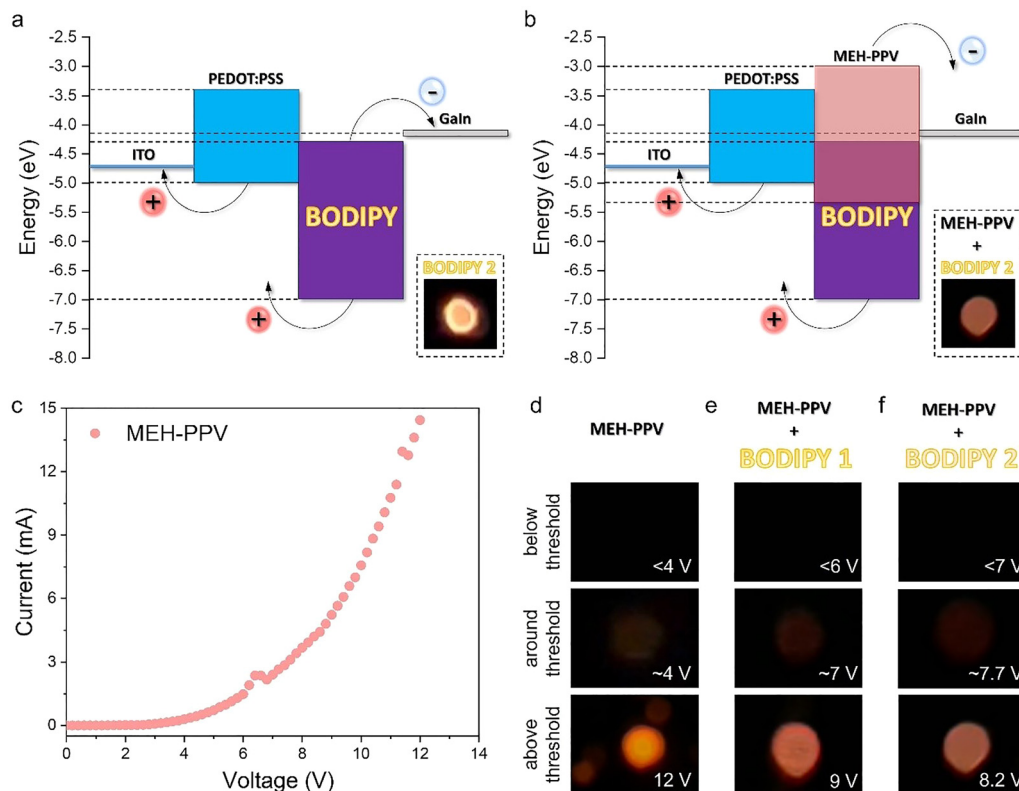
Fig. 10 Energy level diagram of the OLEDs with BODIPY compounds (a), MEH-PPV:BODIPY-doped film (2 wt%) (b) as emitter layer; (c) the current/voltage characteristic of MEH-PPV; (d) observed emissions from MEH-PPV, MEH-PPV + **BDP1** and MEH-PPV + **BDP2**.

preliminary and qualitative manner, the observation of light emission itself is noteworthy, demonstrating that the investigated BODIPY derivatives are capable of electroluminescent behaviour. These findings open promising avenues for further studies, including the extension of these materials to other emission colors and the optimization of device performance.

Finally, the last panels present snapshots corresponding to the applied voltage levels at which the measured current–voltage characteristics are (i) below the electroluminescence threshold (top), (ii) around the threshold (middle), and (iii) above the threshold, where the devices operate at their highest efficiency (bottom), for the MEH-PPV-based OLED, MEH-PPV/**BDP1**, and MEH-PPV/**BDP2** devices, respectively (Fig. 10d–f). These observations demonstrate that (1) BODIPY can serve as the active emission layer and (2) structural variations can induce electroluminescence in simple device configurations. They provide a foundation for further studies aimed at optimizing OLED architectures and quantitatively evaluating device performance.

## 3. Conclusions

As demonstrated by the spectroscopic analysis above, the BODIPY dyes exhibited excellent performance in NLO, basic spectroscopic, and lasing studies, indicating their versatility, further supported by quantum-chemical calculations. Interestingly, compound **BDP2**, theoretically predicted to be the

strongest push–pull system ($\Delta\mu$ = 1.96 D, $\beta_{\text{EFISH}}$ = 5.82 × $10^{-28}$ esu), exhibits the lowest lasing emission threshold ($E_{\text{th}}$ = 65 μJ) and the highest photostability in PMMA, which confirms its efficient CT character and optoelectronic potential. In contrast, **BDP1**, with the lowest $\Delta\mu$ value and first hyperpolarizability, corresponds to a classical, rigid BODIPY core and shows the weakest RL activity – consistent with theoretical predictions for systems lacking CT character. **BDP3**, containing methoxy groups and exhibiting moderate NLO properties, occupies an intermediate position in terms of both the calculated first ($\beta$) and second ($\gamma$) hyperpolarizabilities and the RL intensity. Overall, the observed trends in the absorption parameters ($\lambda$, $\Delta\mu$) correlate well with the predicted and computed NLO activities for **BDP1**–**BDP3**, highlighting a close relationship between molecular structure, linear absorption, and NLO response.

The combined analysis of the photophysical, lasing, and photostability data highlights the central role of the host environment in regulating the optical performance of BODIPY derivatives. The quantum yields in PMMA ($\phi_{\text{fPMMA}}$) are markedly enhanced relative to those in DCM solution, with values of 0.45, 0.27, and 0.88 for **BDP1**–**3**, respectively. This increase is directly reflected in lasing performance: the dyes with the strongest gain in quantum yield (**BDP1** and **BDP2**) exhibit the lowest lasing thresholds in PMMA (96 μJ and 65 μJ, respectively), while **BDP3**, which was already highly emissive in solution, shows a smaller relative improvement. **BDP1** and **BDP3** are more durable in LC

than in PMMA, and **BDP2** constitutes an exception, showing markedly better stability in PMMA. The superior photostability of **BDP1** and **BDP3** in the LC host can be attributed to the hybrid nature of this medium, which combines features of both liquids and solids. On the one hand, the orientational order of the LC phase provides a degree of structural organization that can mitigate nonradiative decay and suppress direct photodegradation pathways. On the other hand, the inherent fluidity of the LC allows for molecular diffusion and exchange, which can redistribute locally degraded species and thereby reduce the cumulative impact of photodamage. This dual character, ordered yet dynamic, supports enhanced photostability compared to a rigid polymer matrix. In contrast, the exceptional behaviour of **BDP2**, which shows higher stability in PMMA, may be rationalized by the formation of more stable, microcrystalline domains in the polymer matrix. Such ordered aggregates can stabilize molecular conformations and restrict detrimental relaxation channels, effectively shielding the dye molecules from photodegradation. As a result, **BDP2** benefits more from the rigid, semi-crystalline environment of PMMA than from the fluid LC host.

Importantly, preliminary OLED experiments incorporating BODIPY dyes revealed indications of electroluminescent behaviour in both pure and MEH-PPV-doped configurations. These initial observations suggest that the structural features enabling efficient lasing and NLO activity may also be relevant under electrical excitation, pointing to the potential of these dyes as multifunctional materials bridging optical gain and electroluminescence.

In conclusion, the present study provides one of the rare demonstrations of BODIPY systems combining efficient lasing, good NLO response, and preliminary results of electroluminescence within a single molecular platform, highlighting their exceptional promise for future integrated photonic and optoelectronic technologies.

## 4. Methods

### 4.1. Synthesis

All reagents were either prepared following synthetic methods found in literature or purchased from commercially available suppliers and used without further purification. The reaction progress and conversion were monitored using gas chromatography (GC) (Agilent 6890N equipped with a flame ionization detector (FID) and a mass spectrometer with electron ionization (EI), model: Agilent MSD5973N, USA), as well as thin-layer chromatography (TLC) (silica gel 60 with fluorescent indicator on aluminium, Macherey-Nagel, Germany). Intermediates and final products were purified using short-path vacuum distillation, column chromatography (normal-phase system with silica gel 100–200 mesh) and crystallization. Structural analysis and purity of the intermediates were determined using gas chromatography. Structural analysis and purity of BODIPY derivatives were determined using $^1$H and $^{13}$C NMR spectra in CDCl$_3$ collected with a Bruker model Avance III spectrometer (Bruker, USA) and high-performance liquid chromatography (HPLC),

Shimadzu Prominence series, model LC20 (Shimadzu, Japan), equipped with two detectors: a diode array detector SPD-M20A and a mass detector LC-MS 2010EV with atmospheric pressure ionization using electrospray ionization technique.

### 4.2. Calculation protocols

The geometry of the ground state (S$_0$) was fully optimized using density functional theory (DFT) with the MN15 functional[95] and the 6-31+G(d) basis set.[96] Solvent effects (DCM) were accounted for using the polarizable continuum model (PCM) in the integral equation formalism variant (IEFPCM).[97] All optimizations were performed without symmetry constraints, and vibrational frequency calculations confirmed that the obtained structures correspond to minima (no imaginary frequencies). The geometry of the first excited state (S$_1$) was optimized using time-dependent DFT (TD-DFT) at the MN15/6-31+G(d) level with IEFPCM (DCM). Frequency calculations ensured that the S$_1$ geometries were true minima on the excited-state potential energy surface. Vertical excitation energies (absorption) were calculated at the optimized S$_0$ geometries using TD-DFT (MN15/6-31+G(d), IEFPCM/DCM). Emission wavelengths were obtained as vertical S$_1$ → S$_0$ transitions calculated at the optimized S$_1$ geometries. All calculations of geometry, frequency, absorption, emission, dipole moments, and first hyperpolarizability $\beta$ ($\beta(0;0,0)$ and $\beta(-2\omega;\omega,\omega)$) were performed using Gaussian 16 Rev C.01.[98] Second hyperpolarizabilities $\gamma$ ($\gamma(0;0,0,0)$ and $\gamma(-3\omega;\omega,\omega,\omega)$) were calculated using Dalton (release Dalton2020.1).[99,100] Both $\beta$ and $\gamma$ values were computed with the range-separated hybrid functional CAM-B3LYP.[101] Calculated second- and third-order hyperpolarizability tensor components ($\beta_{ijk}$ and $\gamma_{ijkl}$), at both static and frequency-dependent regimes, as well as the full Cartesian coordinates of optimized structures, are summarized in the SI (Tables S1–S5).

### 4.3. Sample preparation

**4.3.1. BODIPY dyes in PMMA.** Chosen polymer (PMMA, Aldrich, average $M_w \approx 350\,000$, GPC) was first dissolved in dichloromethane to obtain a 5 wt% stock solution. Each of the BODIPY dyes (**BDP1–3**) was then incorporated individually at a loading of 2 wt% relative to the dry polymer mass. The resulting mixtures were deposited onto glass substrates by drop-casting. After deposition, the films were left to dry in a saturated solvent atmosphere, which facilitated slow evaporation and led to uniform, defect-free thin layers. The measured thicknesses of our solid-state samples were: 28.2, 34.2, and 31.7 µm for **BDP1**, **BDP2**, and **BDP3** in PMMA, respectively. The measurement was performed using the Veeco Dektak-3 Profilometer.

**4.3.2. BODIPY dyes in LC matrices.** The BODIPY dyes were dissolved in the E7 LC mixture in the following ratio: 1.5 mg of BODIPY dye per 0.3 mL of E7 mixture. E7 is a widely used nematic mixture due to its high optical anisotropy and broad temperature range of the nematic phase, which extends from room temperature up to the nematic-to-isotropic transition at 58 °C. The mixture consists of four constituents: 51% 4-cyano-4′-$n$-pentyl-1,1′-biphenyl (5CB), 25% 4-cyano-4′-$n$-heptyl-1,1′-biphenyl (7CB), 16% 4-cyano-4′-$n$-octyloxy-1,1′-biphenyl (8OCB), and 8% 4-cyano-4″-$n$-pentyl-1,1′,1″-terphenyl (5CT) by weight. At room temperature,

5CB and 7CB are viscous liquids, whereas 8OCB and 5CT are solids. This composition ensures the formation of a stable nematic phase at ambient conditions suitable for optical experiments and laser studies.[102–104]

The host–guest solution was combined, mixed, and heated to a temperature of 70 °C, then injected with a microliter pipette into an LC cell with homogeneous orientation, made from two ITO glass slides measuring 11 × 11 mm, with a 30 μm gap between the slides (purchased at the Military University of Technology, Warsaw, Poland).

### 4.4. Basic spectroscopy

Absorption measurements of LC cells and PMMA thin films were carried out at room temperature using a Shimadzu UV-1800 spectrophotometer. Steady-state fluorescence spectra were collected with a Horiba Fluoromax-4 spectrofluorometer. The instrumental resolution was set to 0.5 nm for absorption and 1.0 nm for emission scans.

For DCM solutions, the spectral analyses were carried out at room temperature and in spectrally pure DCM (Thermo Fisher Scientific, USA) with a concentration of approximately $10^{-5}$ mol $dm^{-3}$ using a UV-Vis-NIR 3600 spectrophotometer (Shimadzu, Japan) and a FS5 spectrofluorometer (Edinburgh Instruments, UK). The spectral resolution was set to 0.5 nm for absorption and 1.0 nm for emission measurements. The excitation wavelength for emission measurements was set to 485 nm for **BDP1–2** and 490 nm for **BDP3**. Absolute quantum yield of fluorescence measurements in DCM solutions were performed using a calibrated integrating sphere (SC-30 module for FS5 spectrofluorometer) in quartz cuvettes with an optical path of 1 cm, from solutions in spectrally pure DCM with an absorbance of 0.1 ± 0.01. The excitation wavelengths were set to 477 nm for **BDP1–2** and 485 nm for **BDP3**.

Fluorescence quantum yields of the PMMA thin films containing **BDP1–3** were determined using a calibrated integrating sphere system (GigaHertz Optik, UPB-150-ARTA; 150 mm diameter, $BaSO_4$ coating) designed for reflection, transmission, and absorption measurements. The relative measurements were carried out directly on the prepared thin-film samples under continuous-wave excitation with a 405 nm diode laser (MDL-C-405, 50 mW).

### 4.5. Light amplification

For the lasing studies, a triple-frequency Nd:YAG pulsed laser (Surelite II, Coherent) was used, featuring a pulse duration of 6 ns and a repetition rate of 10 Hz, in combination with a highly efficient mid-band optical parametric oscillator (OPO, Horizon by Continuum). Dyes embedded in PMMA matrices were excited using a 405 nm laser, whereas in LC, the excitation wavelengths were 465 nm for **BDP1** and 475 nm for **BDP2** and **BDP3**. The excitation beam was shaped into a stripe of 6.5 × 0.8 mm using a slit and a cylindrical lens to focus the light, and then directed onto the sample. For each measurement, the emission spectrum was derived as the average of five consecutive laser shots to ensure reproducibility. The incident laser power was recorded with a calibrated energy meter (Coherent

Field Max II) equipped with a J-10MB-HE sensor. To reduce losses and reabsorption, the emitted light was collected from the sample edge *via* an optical fiber and examined using a high-resolution spectrometer (Andor Shamrock SR-500i-B1-R, 0.1 nm resolution) connected to a computer.

The Li–Lo technique determines the lasing threshold by comparing the integrated emission intensity to the input light, using linear fits to the pre- (fluorescence) and post-lasing regions to locate the inflection point marking the onset of lasing.[105]

### 4.6. Harmonics of light generation

To examine the SHG and THG responses of the studied materials, we utilized an experimental setup similar to that reported in our earlier work.[106] In summary, a picosecond Nd:YAG laser (EKSPLA, PL2250 Series) operating at a wavelength of 1064 nm (pulse duration: 30 ps, repetition rate: 10 Hz) served as the excitation source. The beam was directed onto the sample and simultaneously routed to optoelectronic components to trigger signal acquisition. Beam polarization and power were adjusted using a combination of polarizers and a half-wave plate. The materials were prepared as thin films *via* spin-coating and mounted on a motorized stage that allowed precise angular rotation from −70° to +70° with respect to the beam's normal incidence. In addition, before performing the SHG measurements, a corona poling process, a thermo-electric technique used to induce non-centrosymmetry in all samples, was applied. The procedure involved first heating the samples to 100 °C, then applying an electric field of 7 kV for 10 minutes while maintaining the temperature. After switching off the heating system, the samples were kept under the same DC field for an additional 1–2 hours until they reached room temperature. Subsequently, the SHG measurements were carried out. This configuration enabled the use of the Maker fringes technique for quantitative analysis, employing suitable reference samples and theoretical fitting models.

### 4.7. Morphological studies

Optical imaging was carried out using a combination of techniques, including crossed-polarization and photoluminescence, with an Olympus BX60 microscope fitted with a UplanFL 10× objective and a 360 nm excitation source. This approach enabled a detailed morphological characterization of the samples. All imaging was performed at room temperature using the same instrumentation employed for spectroscopic analyses (lasing, absorption, and fluorescence), ensuring consistent and optimal illumination of the excitation region.

Morphological characterization of BODIPY-doped PMMA and LC systems was performed in bright-field mode using a Nikon ECLIPSE Ti2-E inverted microscope. A Nikon CFI60 Plan Fluor 10× objective (N.A. 0.30, W.D. 16 mm) was selected to provide high spatial resolution (∼1 μm) while maintaining a long working distance, allowing safe imaging of fragile or non-planar samples without physical contact. Images were recorded with a monochrome Nikon Qi2 camera (16.25 MP), enabling detailed visualization of microcracks, aggregates, and crystalline domains.

### 4.8. Simple OLED structure

PEDOT:PSS (conductive grade, 1.3 wt% aqueous dispersion), ITO coated glass substrates (surface resistivity 70–100 $\Omega$ sq$^{-1}$), MEH-PPV (average molecular weight $M_n$ 40 000–70 000), and eutectic gallium–indium alloy (Ga 75.5%, In 24.5%) were all obtained from Merck.

Before use, the ITO substrates were cleaned by sequential ultrasonication in detergent, deionized water, isopropyl alcohol (IPA), and acetone for a total of 30 minutes. PEDOT:PSS was deposited onto the cleaned ITO substrates *via* spin coating at 8000 rpm for 30 seconds, followed by thermal annealing at 100 °C for 15 minutes in ambient air. For the BODIPY solution (5 mg mL$^{-1}$ in chloroform) was spin-coated onto the PEDOT:PSS layer at 2000 rpm for 30 seconds and left to dry for 10 minutes. For the MEH-PPV:BODIPY blend film (2 wt% BODIPY), BODIPY was added to the MEH-PPV to create a homogeneous 5 mg mL$^{-1}$ solution in chloroform and then spin-coated onto the PEDOT:PSS layer at 2000 rpm for 30 seconds and left to dry for 10 minutes. Finally, a droplet of GaIn alloy was applied as the top electrode. The current–voltage ($I$–$V$) characteristics of the electroluminescent OLED devices were recorded using a Keithley 2280S-60-3 source meter unit.

## Conflicts of interest

There are no conflicts to declare.

## Data availability

The authors state that the data supporting the findings of this study are included within the paper and its supplementary information (SI) files. Supplementary information contains synthetic procedures, simulated absorption/emission spectra, RMSD and $\beta/\gamma$ tensor data for **BDP1–3**, plus experimental results: photophysical parameters, FWHM and Stokes shift comparisons, bright-field images of BODIPY-doped PMMA/LC films, and $I$–$V$ characteristics for **BDP1** and **BDP3**. See DOI: https://doi.org/10.1039/d5tc03584h.

Any raw data required in a different format can be obtained from the corresponding author upon reasonable request. Source data are also provided with this paper.

## Acknowledgements

## References

1  G. Huseynova, *Mater. Sci. Eng. Int. J.*, 2020, **4**, 166–167.

2  J. Khan, R. T. M. Ahmad, J. Tan, R. Zhang, U. Khan and B. Liu, *SmartMat*, 2023, **4**, e1156, DOI: **10.1002/smm2.1156**.

3  X. Xu, L. Sun, K. Shen and S. Zhang, *Synth. Met.*, 2019, **256**, 116137, DOI: **10.1016/j.synthmet.2019.116137**.

4  Y. Chen, M. He, J. Peng, Y. Sun and Z. Liang, *Adv. Sci.*, 2016, **3**, 1500392, DOI: **10.1002/advs.201500392**.

5  G. A. Nowsherwan, Q. Ali, U. F. Ali, M. Ahmad, M. Khan and S. S. Hussain, *Organics*, 2024, **5**, 520–560.

6  Y. Shirota and H. Kageyama, in *Handbook of Organic Materials for Electronic and Photonic Devices*, ed. O. Ostroverkhova, Woodhead Publishing, Cambridge, 2nd edn, 2019, vol. 1(1), pp. 3–42.

7  F. J. Duarte, *Opt. Photonics News*, 2003, **14**, 20–25.

8  A. Machnev, D. Ofer, I. Shishkin, V. Kozlov, C. Diaferia, A. Accardo, G. Morelli, B. Apter, A. Inberg, G. Rosenman and P. Ginzburg, *Sci. Rep.*, 2021, **11**, 17609, DOI: **10.1038/s41598-021-96982-5**.

9  J. Mysliwiec, K. Cyprych, L. Sznitko and A. Miniewicz, *J. Opt.*, 2017, **19**, 033003, DOI: **10.1088/2040-8986/aa53fb**.

10  Y. Wang, Z. Duan, Z. Qiu, P. Zhang, J. Wu, D. Zhang and T. Xiang, *Sci. Rep.*, 2017, **7**, 8385, DOI: **10.1038/s41598-017-08625-3**.

11  F. Yao, R. Hong, B. Zhang, Y. Pei, C. Hou and X. Sun, *Opt. Lett.*, 2020, **45**, 6118–6121.

12  M. Poddar and R. Misra, *Coord. Chem. Rev.*, 2020, **421**, 213462, DOI: **10.1016/j.ccr.2020.213462**.

13  K. Rurack and M. Spieles, *Anal. Chem.*, 2011, **83**, 1232–1242.

14  K. Umezawa, Y. Nakamura, H. Makino, D. Citterio and K. Suzuki, *J. Am. Chem. Soc.*, 2008, **130**, 1550–1551.

15  S. K. Keshri, K. Mandal, Y. Kumar, D. Yadav and P. Mukhopadhyay, *Chem. – Eur. J.*, 2021, **27**, 6954–6962.

16  C. Mowatt, S. M. Morris, M. H. Song, T. D. Wilkinson, R. H. Friend and H. J. Coles, *J. Appl. Phys.*, 2010, **107**, 043101, DOI: **10.1063/1.3284939**.

17  R. M. Christie, in *Fluorescent dyes, w Handbook of Textile and Industrial Dyeing: Principles, Processes and Types of Dyes*, ed. M. Clark, Woodhead Publishing, Cambridge, UK, 2011, vol. 1(17), pp. 562–587.

18  W. Cheng, H. Chen, C. Liu, C. Ji, G. Ma and M. Yin, *View*, 2020, **1**, 20200055, DOI: **10.1002/VIW.20200055**.

19  K. Nowak, I. Karampinis and A. L. H. Gerken, *Visc. Med.*, 2020, **36**, 80–87.

20  A. Kamkaew, S. H. Lim, H. B. Lee, L. V. Kiew, L. Y. Chung and K. Burgess, *Chem. Soc. Rev.*, 2013, **42**, 77–88.

21  P. P. Kumar, S. Saxena and R. Joshi, *Colorants*, 2025, **4**, 13, DOI: **10.3390/colorants4020013**.

22  J. Bañuelos, *Chem. Rec.*, 2016, **16**, 335–348.

23  S. V. Dzyuba, *Biosensors*, 2020, **10**, 192, DOI: **10.3390/bios10120192**.

24  G. Ulrich, R. Ziessel and A. Harriman, *Angew. Chem., Int. Ed.*, 2008, **47**, 1184–1201.

25  N. Adarsh, M. Shanmugasundaram, R. R. Avirah and D. Ramaiah, *Chem. – Eur. J.*, 2012, **18**, 12655–12662.

26  X.-F. Zhang, G. Q. Zhang and J. Zhu, *J. Fluoresc.*, 2019, **29**, 407–416.

27  Y. Zhang, L. Tian, W. Zhao, L. Gai and H. Lu, *J. Mol. Struct.*, 2025, **1347**, 143305, DOI: **10.1016/j.molstruc.2025.143305**.

28  S. Zhu, J. Zhang, G. Vegesna, F.-T. Luo, S. A. Green and H. Liu, *Org. Lett.*, 2011, **13**, 438–441.

29  A. J. C. Kuehne and M. C. Gather, *Chem. Rev.*, 2016, **116**, 12823–12864.

30  I. Zubair, R. A. Khera, A. Naveed, R. A. Shehzad and J. Iqbal, *Mater. Sci. Semicond. Process.*, 2022, **148**, 106812, DOI: **10.1016/j.mssp.2022.106812**.

31  D. Pinjari, Y. Patil and R. Misra, *Chem. – Asian J.*, 2024, **19**(15), e202400167, DOI: **10.1002/asia.202400167**.

32  A. Maity, A. Sarkar, S. B. N. Bhaktha and S. K. Patra, *New J. Chem.*, 2020, **44**, 14650–14661.

33  I. García-Moreno, F. Amat-Guerri, M. Liras, A. Costela, L. Infantes, R. Sastre, F. López Arbeloa, J. Bañuelos Prieto and Í. López Arbeloa, *Adv. Funct. Mater.*, 2007, **17**, 3088–3098.

34  M. Álvarez, A. Costela, I. García-Moreno, F. Amat-Guerri, M. Liras, R. Sastre, F. López Arbeloa, J. Bañuelos Prieto and I. López Arbeloa, *Photochem. Photobiol. Sci.*, 2008, **7**, 802–813.

35  G. Duran-Sampedro, A. R. Agarrabeitia, I. Garcia-Moreno, A. Costela, J. Bañuelos, T. Arbeloa, I. López Arbeloa, J. L. Chiara and M. J. Ortiz, *Eur. J. Org. Chem.*, 2012, 6335–6350.

36  A. Prakash, J. C. Janardhanan, V. K. Praveen, P. Radhakrishnan and A. Mujeeb, *J. Lumin.*, 2022, **252**, 119343, DOI: **10.1016/j.jlumin.2022.119343**.

37  H. Kang, J. Ye, H. Wang, Y. Zhang and Y. Qiu, *Theor. Chem. Acc.*, 2021, **140**, 47.

38  G. Ulrich, A. Barsella, A. Boeglin, S. Niu and R. Ziessel, *ChemPhysChem*, 2014, **15**, 2693–2700.

39  H. Chang, M. V. Bondar, N. Munera, S. David, O. Maury, G. Berginc, B. Le Guennic, D. Jacquemin, C. Andraud, D. J. Hagan and E. W. Van Stryland, *Chem. – Eur. J.*, 2022, **28**, e202104072, DOI: **10.1002/chem.202104072**.

40  B. Kulyk, S. Taboukhat, H. Akdas-Kilig, J.-L. Fillaut, M. Karpierz and B. Sahraoui, *Dyes Pigm.*, 2017, **137**, 507–511.

41  S. S. Thakare, M. C. Sreenath, S. Chitrambalam, I. H. Joe and N. Sekar, *Opt. Mater.*, 2017, **64**, 453–460.

42  H.-Q. Wang, J.-T. Ye, Y. Zhang, Y.-Y. Zhao and Y.-Q. Qiu, *J. Mater. Chem. C*, 2019, **7**, 7531–7547.

43  M. Chapran, E. Angioni, N. J. Findlay, B. Breig, V. Cherpak, P. Stakhira, T. Tuttle, D. Volyniuk, J. V. Grazulevicius, Y. A. Nastishin, O. D. Lavrentovich and P. J. Skabara, *ACS Appl. Mater. Interfaces*, 2017, **9**, 4750–4757.

44  C.-L. Liu, Y. Chen, D. P. Shelar, C. Li, G. Cheng and W.-F. Fu, *J. Mater. Chem. C*, 2014, **2**, 5471.

45  T. Nakamura, H. Sasabe, S. Abe, K. Kumada, R. Sugiyama, T. Hanayama and J. Kido, *Mol. Syst. Des. Eng.*, 2023, **8**, 866–873.

46  B. M. Squeo and M. Pasini, *Supramol. Chem.*, 2020, **32**, 56–70.

47  D. A. Merkushev, S. D. Usoltsev, Yu. S. Marfin, A. P. Pushkarev, D. Volyniuk, J. V. Grazulevicius and E. V. Rumyantsev, *Mater. Chem. Phys.*, 2017, **187**, 104–111.

48  A. Khan, F.-C. Kong, J. Kazmi, S. Kumar, T. Leydecker and Z. Wang, *J. Mater. Chem. C*, 2025, **13**, 5624–5632.

49  U. Simon and F. K. Tittel, in *Experimental Methods in the Physical Sciences*, ed. F. B. Dunning and R. G. Hulet, Academic Press, 1997, vol. 29C(9), pp. 231–278.

50  W. Jaffray, F. Belli, S. Stengel, M. A. Vincenti, M. Scalora, M. Clerici, V. M. Shalaev, A. Boltasseva and M. Ferrera, *Adv. Opt. Mater.*, 2024, **12**(8), 2401249.

51  F. Castet, V. Rodriguez, J.-L. Pozzo, L. Ducasse, A. Plaquet and B. Champagne, *Acc. Chem. Res.*, 2013, **46**, 2656–2665.

52  A. Zawadzka, P. Płóciennik, J. Strzelecki and B. Sahraoui, *Opt. Mater.*, 2014, **37**, 327–337.

53  C. B. Greenberg, *Thin Solid Films*, 1994, **251**, 81–93.

54  J. M. Hales, S. Barlow, H. Kim, S. Mukhopadhyay, J.-L. Brédas, J. W. Perry and S. R. Marder, *Chem. Mater.*, 2014, **26**, 549–560.

55  S. D. Cox, T. E. Gier, G. D. Stucky and J. Bierled, *J. Am. Chem. Soc.*, 1988, **110**, 2987–2988.

56  S. P. Karna, P. N. Prasad and M. Dupuis, *J. Chem. Phys.*, 1991, **94**, 1171–1181.

57  E. Peña-Cabrera, A. Aguilar-Aguilar, M. González-Domínguez, E. Lager, R. Zamudio-Vázquez, J. Godoy-Vargas and F. Villanueva-García, *Org. Lett.*, 2007, **9**, 3985–3988.

58  A. Vyšniauskas, I. López-Duarte, N. Duchemin, T.-T. Vu, Y. Wu, E. M. Budynina, Y. A. Volkova, E. Peña Cabrera, D. E. Ramírez-Ornelas and M. K. Kuimova, *Phys. Chem. Chem. Phys.*, 2017, **19**, 25252–25259.

59  R. W. Wagner and J. S. Lindsey, *Pure Appl. Chem.*, 1996, **68**, 1373–1380.

60  J. S. Lindsey, *Acc. Chem. Res.*, 2010, **43**, 300–311.

61  R. Ziessel, G. Ulrich and A. Harriman, *New J. Chem.*, 2007, **31**, 496–501.

62  A. Loudet and K. Burgess, *Chem. Rev.*, 2007, **107**, 4891–4932.

63  S. Xuan, N. Zhao, X. Ke, Z. Zhou, F. R. Fronczek, K. M. Kadish, K. M. Smith and M. G. H. Vicente, *J. Org. Chem.*, 2017, **82**, 2545–2557.

64  T. Gayathri, A. K. Barui, S. Prashanthi, C. R. Patra and S. P. Singh, *RSC Adv.*, 2014, **4**, 47409–47413.

65  S. R. Marder, L.-T. Cheng, B. G. Tiemann, A. C. Friedli, M. Blanchard-Desce, J. W. Perry and J. Skindhøj, *Science*, 1994, **263**, 511–514.

66  P. N. Prasad and D. J. Williams, *Introduction to nonlinear optical effects in molecules and polymers*, Wiley, New York, 1991.

67  S. Figueredo López, M. Páez Meza and F. Torres Hoyos, *Comput. Theor. Chem.*, 2018, **1133**, 25–32.

68  J. L. Oudar, *J. Chem. Phys.*, 1977, **67**, 446–457.

69  F. Nisic, A. Colombo, C. Dragonetti, M. Fontani, D. Marinotto, S. Righetto, D. Roberto and J. A. G. Williams, *J. Mater. Chem. C*, 2015, **3**, 7421–7427.

70  F. Limosani, F. Tessore, A. Forni, A. Lembo, G. Di Carlo, C. Albanese, S. Bellucci and P. Tagliatesta, *Materials*, 2023, **16**, 5427, DOI: **10.3390/ma16155427**.

71  F. Bureš, *RSC Adv.*, 2014, **4**, 58826–58851.

72  J. Zyss and I. Ledoux, *Chem. Rev.*, 1994, **94**, 77–105.

73 S. R. Marder, J. W. Perry and W. P. Schaefer, *Science*, 1989, **245**, 626–628.

74 L. R. Dalton, A. W. Harper, R. Ghosn, W. H. Steier, M. Ziari, H. Fetterman, Y. Shi, R. V. Mustacich, A. K.-Y. Jen and K. J. Shea, *Chem. Mater.*, 1995, **7**, 1060–1081.

75 D. Frath, J. Massue, G. Ulrich and R. Ziessel, *Angew. Chem., Int. Ed.*, 2014, **53**, 2290–2310.

76 R. W. Boyd, *Nonlinear optics*, Academic Press, London, 2nd edn, 2003.

77 K. Waszkowska, M. Busch, S. Slassi, A. Amine, A. El-Ghayoury, J. Strzelecki, A. Zawadzka, A. V. Kityk, P. Huber and B. Sahraoui, *Adv. Opt. Mater.*, 2025, **13**(30), e00975.

78 F. Kajzar, Y. Okada-Shudo, C. Meritt and Z. Kafafi, *Synth. Met.*, 2001, **117**, 189–193.

79 U. Gubler and C. Bosshard, *Phys. Rev. B: Condens. Matter Mater. Phys.*, 2000, **61**, 10702–10710.

80 M. Rodríguez, J. L. Maldonado, G. Ramos-Ortíz, O. Domínguez, Ma. E. Ochoa, R. Santillan, N. Farfán, M.-A. Meneses-Nava and O. Barbosa-García, *Polyhedron*, 2012, **43**, 194–200.

81 *Progress in the Science of Functional Dyes*, ed. Y. Ooyama and S. Yagi, Springer, Singapore, 2021.

82 L. Jiao, C. Yu, J. Wang, E. A. Briggs, N. A. Besley, D. Robinson, M. J. Ruedas-Rama, A. Orte, L. Crovetto, E. M. Talavera, J. M. Alvarez-Pez, M. Van der Auweraer and N. Boens, *RSC Adv.*, 2015, **5**, 89375–89388.

83 K. Lupinska, S. Kotowicz, A. Grabarz, M. Siwy, K. Sulowska, S. Mackowski, L. Bu, Y. Bretonnière, C. Andraud, E. Schab-Balcerzak and L. Sznitko, *ACS Omega*, 2024, **9**, 40769–40782.

84 D. Zhang, V. Martín, I. García-Moreno, A. Costela, M. E. Pérez-Ojeda and Y. Xiao, *Phys. Chem. Chem. Phys.*, 2011, **13**, 13026–13033.

85 M. E. Pérez-Ojeda, C. Thivierge, V. Martín, Á. Costela, K. Burgess and I. García-Moreno, *Opt. Mater. Express*, 2011, **1**, 243–251.

86 J. Bañuelos, V. Martín, C. F. A. Gómez-Durán, I. J. A. Córdoba, E. Peña-Cabrera, I. García-Moreno, Á. Costela, M. E. Pérez-Ojeda, T. Arbeloa and Í. L. Arbeloa, *Chem. – Eur. J.*, 2011, **17**, 7261–7270.

87 Y. Yang, L. Zhang, C. Gao, L. Xu, S. Bai and X. Liu, *RSC Adv.*, 2014, **4**, 38119–38123.

88 A. Maity, A. Sarkar, A. Sil, S. B. N. Bhaktha and S. K. Patra, *New J. Chem.*, 2017, **41**, 2296–2308.

89 K. K. Jagtap, N. Shivran, S. Mula, D. B. Naik, S. K. Sarkar, T. Mukherjee, D. K. Maity and A. K. Ray, *Chem. – Eur. J.*, 2013, **19**, 702–708.

90 L. Sznitko, A. Szukalski, K. Cyprych, P. Karpinski, A. Miniewicz and J. Mysliwiec, *Chem. Phys. Lett.*, 2013, **576**, 31–34.

91 W. N. Sisk, N. Ono, T. Yano and M. Wada, *Dyes Pigm.*, 2002, **55**, 143–150.

92 E. J. Lous, P. W. M. Blom, L. W. Molenkamp and D. M. De Leeuw, *J. Appl. Phys.*, 1997, **81**, 3537–3542.

93 J. Ouyang, Q. Xu, C.-W. Chu, Y. Yang, G. Li and J. Shinar, *Polymer*, 2004, **45**, 8443–8450.

94 Z. Zheng, Q. Dong, L. Gou, J.-H. Su and J. Huang, *J. Mater. Chem. C*, 2014, **2**, 9858–9865.

95 H. S. Yu, X. He, S. L. Li and D. G. Truhlar, *Chem. Sci.*, 2016, **7**, 5032–5051.

96 R. Ditchfield, W. J. Hehre and J. A. Pople, *J. Chem. Phys.*, 1971, **54**, 724–728.

97 S. Miertus, E. Scrocco and J. Tomasi, *Chem. Phys.*, 1981, **55**, 117–129.

98 M. J. Frisch, G. W. Trucks, H. B. Schlegel, G. E. Scuseria, M. A. Robb, J. R. Cheeseman, *et al.*, *Gaussian 16 (Revision C.01)*, Wallingford, CT, 2016.

99 K. Aidas, C. Angeli, K. L. Bak, V. Bakken, R. Bast, L. Boman, O. Christiansen, R. Cimiraglia, S. Coriani, P. Dahle, E. K. Dalskov, U. Ekstrom, T. Enevoldsen, J. J. Eriksen, P. Ettenhuber, B. Fernandez, L. Ferrighi, H. Fliegl, L. Frediani, K. Hald, A. Halkier, C. Hättig, H. Heiberg, T. Helgaker, A. C. Hennum, H. Hettema, E. Hjertenas, S. Host, I-M. Hayvik, M. F. Iozzi, B. Jansik, H. J. A. Jensen, D. Jonsson, P. Jorgensen, J. Kauczor, S. Kirpekar, T. Kjergaard, W. Klopper, S. Knecht, R. Kobayashi, H. Koch, J. Kongsted, A. Krapp, K. Kristensen, A. Ligabue, O. B. Lutnis, J. I. Melo, K. V. Mikkelsen, R. H. Myhre, C. Neiss, C. B. Nielsen, P. Norman, J. Olsen, J. M. H. Olsen, A. Osted, M. J. Packer, F. Pawlowski, T. B. Pedersen, P. F. Provasi, S. Reine, Z. Rinkevicius, T. A. Ruden, K. Ruud, V. V. Rybkin, P. Salek, C. C. M. Samson, A. S. de Meras, T. Saue, S. P. A. Sauer, B. Schimmelpfennig, K. Sneskov, A. H. Steindal, K. O. Sylvester-Hvid, P. R. Taylor, A. M. Teale, E. I. Tellgren, D. P. Tew, A. J. Thorvaldsen, L. Thogersen, O. Vahtras, M. A. Watson, D. J. D. Wilson, M. Ziolkowski and H. Ågren, *Wiley Interdiscip. Rev.:Comput. Mol. Sci.*, 2014, **4**, 269–284.

100 Dalton, a molecular electronic structure program, Release Dalton 2020.1, 2022, **https://daltonprogram.org**.

101 T. Yanai, D. P. Tew and N. C. Handy, *Chem. Phys. Lett.*, 2004, **393**, 51–57.

102 G. Vijayakumar, M. J. Lee, M. Song, S.-H. Jin, J. W. Lee, C. W. Lee, Y.-S. Gal, H. J. Shim, Y. Kang, G.-W. Lee, K. Kim, N.-G. Park and S. Kim, *Macromol. Res.*, 2009, **17**, 963–968.

103 A. Mouquinho, M. Saavedra, A. Maiau, K. Petrova, M. T. Barros, J. L. Figueirinhas and J. Sotomayor, *Mol. Cryst. Liq. Cryst.*, 2011, **542**, 132/[654]–140/[662].

104 A. R. E. Brás, S. Henriques, T. Casimiro, A. Aguiar-Ricardo, J. Sotomayor, J. Caldeira, C. Santos and M. Dionísio, *Liq. Cryst.*, 2007, **34**, 591–597.

105 A. Szukalska, A. Zak, E. Chrzumnicka, A. Gibas, A. Baszczuk and J. Mysliwiec, *Giant*, 2024, **18**, 100279, DOI: **10.1016/j.giant.2024.100279**.

106 A. Szukalski, Y. Cheret, A. M. Grabarz, A. El-Ghayoury and B. Sahraoui, *Adv. Opt. Mater.*, 2025, **13**(10), 2402946.